Chapter 2

A Novel Soft-Switched Triangular Modulation for DC-AC Dual Active Bridge

2.1 Introduction

In Chapter 1, various types of DAB topologies and modulation techniques were discussed. Those modulation techniques based on TZM and TRM primarily emphasize achieving ZVS during turn-on. Interestingly, the existing literature largely overlooks ZCS, instead focusing heavily on ensuring ZVS, often employing multiple control variables or degrees of freedom (DoF) in the process. While thorough, this approach tends to complicate both the controller's design and its practical implementation.

This chapter presents a novel methodology: a TRM-based variable frequency technique for Matrix-type DC-AC DAB converters, which can be applied in two distinct ways. Unlike the switching technique presented in [120], which modulates the entire H-bridge, this innovative technique focuses on modulating just one leg using a sinusoidally modified variable frequency PWM. This modulation technique achieved true soft switching by precisely controlling the transformer voltage to accurately shape the transformer current through variable frequency operation of the switches. The proposed TRM employs a single carrier and a single control variable/ DoF for it's realization, eliminating the need for complex analytical approaches or optimization techniques.

This significantly reduces complexity and switching delays, simplifying controller design. Additionally, it enhances efficiency across the converter's operational power ranges. Further, this strategy achieves soft-switching across various devices, enables near-unity power factor operation using only single control variable, and ensures precise output regulation. The key contributions of the proposed modulation technique are as follows:

(a) A novel modulation technique where power transfer due to C2C phase shift between variable and fixed frequency PWM of DC bridge using method 1. C2C phase shift between AC and DC bridge operating at 50% duty and fixed frequency using method 2.
(b) PFC during G2V and unity power factor (UPF) operation during V2G with single control variable facilitating simple control of power flow regulation.
(c) ZVS turn ON, ZCS turn OFF for the DC side bridge and ZCS turn ON, OFF for the AC side bridge for the entire envelope of the line frequency.
(d) DSP-based digital realization of the variable frequency modulation technique using a single carrier/counter.

The chapter is organized as follows: Section 2.2 discusses the operation and analysis of the converter using both methods. In Section 2.3, the DSP-based digital realization of the two methods using TMS320F28335 is presented. Section 2.4 presents simulation results, followed by experimental results for V2H and G2V applications using method 1. Section 2.5 examines the dynamic performance of the proposed modulation technique, the soft switching analysis of the proposed modulation and a comparison with existing literature. Finally, Section 2.6 concludes this chapter.

2.2 Converter Topology and Proposed Modulation Technique

The converter topology of a single-phase single-stage matrix-type bidirectional DC to AC dual active bridge converter with a high-frequency AC link is shown in Fig. 2.1. It consists of an H-bridge on the DC side and an AC-to-AC (matrix) converter on the AC side. Both converters are separated by a high-frequency AC link. High-frequency AC link consists of a leakage inductance (L_k) which acts as a power link for both bridges and the transformer has a turns ratio of $N:1$. In Fig. 2.1, leakage inductance is referred to the DC side; however, the position of the leakage inductance is not restricted to the DC side and completely depends upon the application and current rating of both sides. Additionally, the external leakage inductance present in the circuit can be collectively considered as part of the overall leakage inductance of the transformer.

The DC side H-bridge converts DC input to high-frequency AC voltage and vice versa. AC voltage appears across the primary of the transformer before the L_k between nodes A-B, referred to as a primary voltage (v_p). On the secondary side, the AC-to-AC converter is responsible for converting high-frequency AC into line frequency and vice versa during AC-to-DC power transfer. The switching frequency of the matrix-type bidirectional DC to AC DAB is much higher than that of the line frequency. So, the AC signal at line frequency can be assumed to be constant at the switching instance. AC voltage appears across the secondary of the high-frequency transformer between node E-F, referred as secondary voltage (v_p). The voltage reflects the primary side between node C-D after the leakage inductance, referred to as reflected secondary voltage to the primary (v_x), which is equal to v_x=Nv_s. It should be noted that the DC side bridge is referred to as the primary side, and the AC bridge side is referred to as the secondary side. Both DC and AC sides consist of LC filters, namely L_{dc}, C_{dc} in the DC side, and L_{ac}, C_{ac} in the AC side.

Additionally, the switches located in Leg 1 of the primary side are designated as

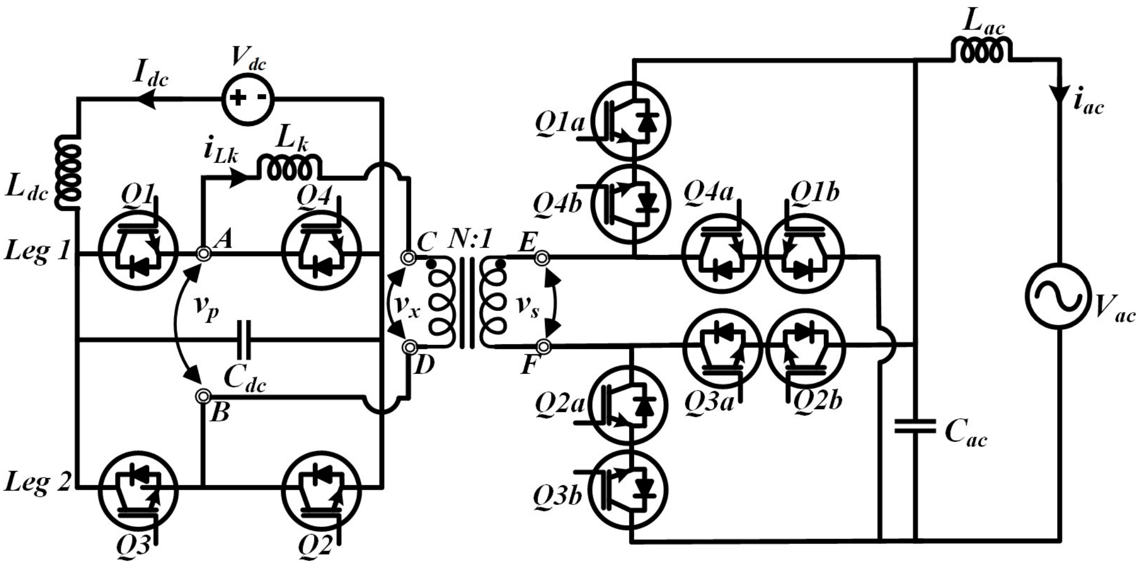

Figure 2.1: Topology of single-phase single-stage matrix-type bidirectional DC to AC dual active bridge converter with high-frequency AC link.

Q1 and Q4, while those in Leg 2 are identified as Q2 and Q3. This labeling helps in clearly distinguishing the switching components within each leg for analysis and control purposes.

2.2.1 Converter Analysis and Operation

DC side H-Bridge has been regulated using a reference sinusoidal AC signal at line frequency, which can be defined by (2.1).

$$m(t) = |V_{ref}| = \left|\frac{Nv_{ac}}{V_{dc}}\right| = \frac{NV_m}{V_{dc}}\,|sin(2\pi ft)| \tag{2.1}$$

where v_{ac} is the desired AC voltage, V_{dc} is the supplied input DC voltage and V_{ref} is the reference signal required for generating the PWM signal for the H-bridge, and $m(t)$ is the duty ratio responsible for generating PWM for the DC side bridge. The maximum value of the duty ratio ($\hat{m}$) is given by (2.2).

$$\hat{m} = \frac{NV_m}{V_{dc}} \tag{2.2}$$

A phase shift term $\pm\Delta t$ is defined between the center/midpoint of the primary side voltage and the center of the secondary side voltage of the transformer over one switching cycle. The sign of Δt is responsible for the direction of the power transferred from one side to the other side. For the analysis, Δt is considered positive when power is transferred from the DC to the AC side, and it is defined by equation (2.3).

$$\Delta t = \frac{\alpha T_s}{4} \tag{2.3}$$

where α is the phase shift ratio and has a range from -(1-$\hat{m}$) to (1-$\hat{m}$). The value of α and $\hat{m}$ are selected in such a way that the width of the primary side transformer voltage should not cross the secondary side transformer voltage. In Fig. 2.2, the principal waveform of the bidirectional DC to AC dual active bridge over one switching cycle (T_s) of the AC side bridge is shown. For the following mathematical analysis, it is assumed that the transformer and switching are ideal. Due to the nature of transformer voltages, the corresponding current (i_{Lk}) flows through the leakage inductance as shown in Fig. 2.2. The voltages that appear across the transformer are assumed to be the same as the instantaneous applied voltages. Assuming v_{ac} to be positive, v_p and v_s is given by the equation (2.4) and (2.5).

$$v_p(t) = \begin{cases} 0, 0 \le t \le \frac{T_s}{4}(1-m-\alpha) \\ V_{dc}, \frac{T_s}{4}(1-m-\alpha) \le \ t \le \frac{T_s}{4}(1+m-\alpha) \\ 0, \frac{T_s}{4}(1+m-\alpha) \le \ t \le \frac{T_s}{4}(3-m-\alpha) \\ -V_{dc}, \frac{T_s}{4}(3-m-\alpha) \le \ t \le \frac{T_s}{4}(3+m-\alpha) \\ 0, \frac{T_s}{4}(3+m-\alpha) \le \ t \le T_s \end{cases} \tag{2.4}$$

$$v_x(t) = \begin{cases} Nv_{ac}, 0 \le t \le \frac{T_s}{2} \\ -Nv_{ac}, \frac{T_s}{2} \le t \le T_s \end{cases} \tag{2.5}$$

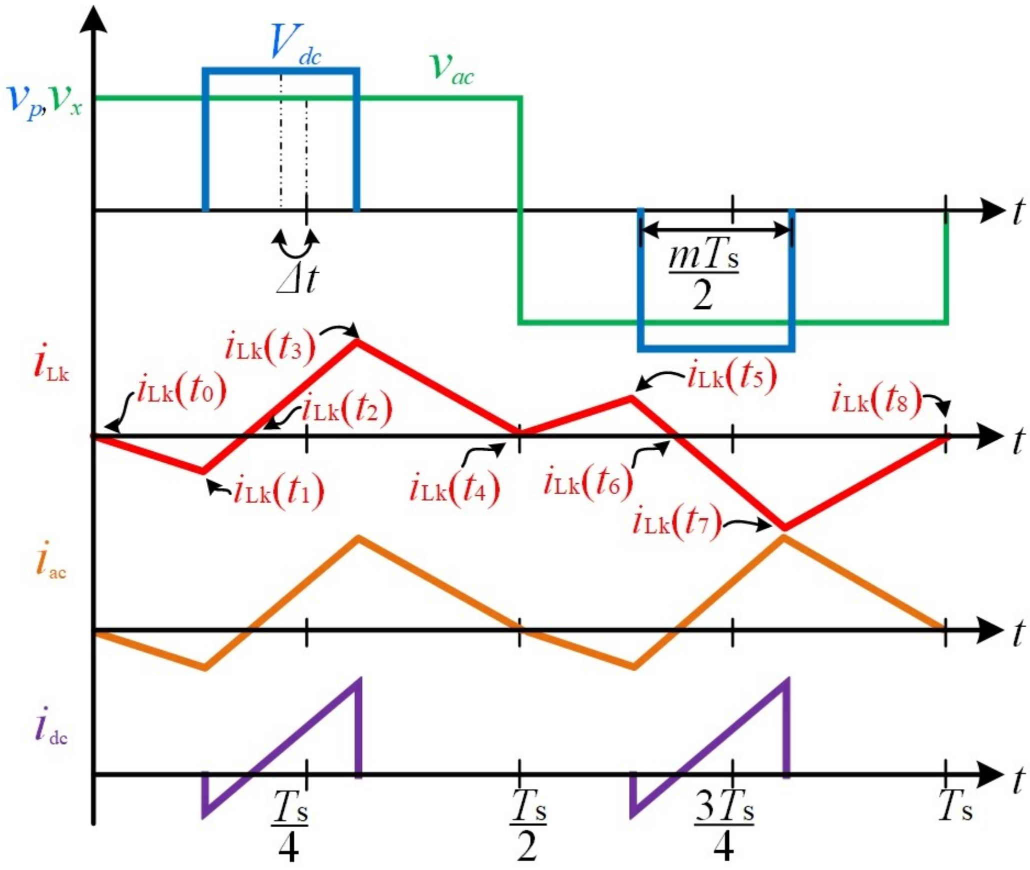

Figure 2.2: Principle operating waveform of bidirectional DC to AC dual active bridge converter.

Assuming the initial current flowing through leakage inductance during the start of the switching cycle to be zero, i.e., $i_{Lk}(t_0)$ =0. Applying inductor volt-second balance on the L_k and using (2.1), (2.4) and (2.5) following are the various instances of the $i_{Lk}(t)$ given by (2.6) to (2.9).

$$i_{Lk}(t_1) = -\frac{Nv_{ac}(1-m-\alpha)}{4f_sL_k} = -\frac{mV_{dc}(1-m-\alpha)}{4f_sL_k} \tag{2.6}$$

$$i_{Lk}(t_3) = \frac{Nv_{ac}(1-m+\alpha)}{4f_sL_k} = \frac{mV_{dc}(1-m+\alpha)}{4f_sL_k} \tag{2.7}$$

$$i_{Lk}(t_5) = -i_{Lk}(t_1) \tag{2.8}$$

$$i_{Lk}(t_7) = -i_{Lk}(t_3) \tag{2.9}$$

Considering the waveform of i_{Lk} between t_1 to t_3 in Fig. 2.2, the following condition is true.

$$\left|\frac{i_{Lk}(t_1)}{t_2 - t_1}\right| = \left|\frac{i_{Lk}(t_3)}{t_3 - t_2}\right| \tag{2.10}$$

$$t_3 - t_1 = \frac{mT_s}{2} \tag{2.11}$$

Using (2.6), (2.7), (2.11) and solving (2.10), values of the t_2 and t_3 are given by (2.12) and (2.13).

$$t_2 = \frac{mT_s(1 - m - \alpha)}{4(1 - m)} \tag{2.12}$$

$$t_3 = \frac{T_s}{4}(1 + m + \alpha) \tag{2.13}$$

t_2 and t_6 are the time instants at which i_{Lk} is zero before commutation. The average ac currents ($\bar{i}_{ac}$) over the one switching cycle are given by (2.14).

$$\bar{i}_{ac} = \frac{2}{T_s}\left(\frac{1}{2} \cdot -i_{Lk}(t_1) \cdot (t_2 - t_0) + \frac{1}{2} \cdot i_{Lk}(t_3) \cdot (t_4 - t_2)\right) \tag{2.14}$$

Simplifying (2.14), $\bar{i}_{ac}$ over half cycle of line frequency becomes (2.15).

$$\bar{i}_{ac} = \frac{N\alpha V_{dc}}{4L_k f_s} m(t) \tag{2.15}$$

$\bar{i}_{ac}$ is a function of $m(t)$ and is in phase with v_{ac}; hence near unity power factor can be achieved using this modulation technique. Similarly, the average DC current ($\bar{i}_{dc}$) over one switching cycle is given by (2.16).

$$\bar{i}_{dc} = \frac{2}{T_s}(\frac{1}{2} \cdot (i_{Lk}(t_3) - i_{Lk}(t_1)) \cdot (t_3 - t_1)) \tag{2.16}$$

Simplifying (2.16), $\bar{i}_{dc}$ over half cycle of line frequency becomes (2.17).

$$\bar{i}_{dc} = \frac{N\alpha v_{ac}}{4L_k f_s} m(t) \tag{2.17}$$

From (2.15) and (2.17), it can be observed that both are a function of $m(t)$ which is the absolute value of V_{ref}, however, switching of AC to AC converter carried out in such a way that bounded value at the line frequency will appear at the load side. Using power balance, the output power can be calculated using any current equation, and it is given by (2.18).

$$\bar{P}_{dc} = \frac{\alpha V_m^2}{4L_k f_s} sin^2(2\pi f t) \tag{2.18}$$

Power can be varied by varying the phase shift ratio, and it is a linear function of the control variable. Power delivered by the converter during various intervals is shown in Table 2.1.

Table 2.1: Power Delivered by the Converter During Various Time Intervals

Time Interval	**Power delivered**
$t_0 - t_1$	$\left\lvert \frac{mN^2 v_{ac} V_{dc}(1-m-\alpha)^2}{16 f_s L_k} \right\rvert$
$t_1 - t_2$	$\left\lvert \frac{m^2 N^2 v_{ac} V_{dc}(1-m-\alpha)^2}{16(1-m) f_s L_k} \right\rvert$
$t_2 - t_3$	$\left\lvert \frac{m^2 N^2 v_{ac} V_{dc}(1-m+\alpha)^2}{16(1-m) f_s L_k} \right\rvert$
$t_3 - t_4$	$\left\lvert \frac{mN^2 v_{ac} V_{dc}(1-m+\alpha)^2}{16 f_s L_k} \right\rvert$

2.2.2 Modulation Technique Using Method 1

The modulation technique using method 1 can be acknowledged using Fig. 2.3. In Fig. 2.3, the principal operating waveform along with various gating signals has been shown for both $v_{ac} > 0$ and $v_{ac} < 0$. The gating signal for leg 1 is the same as that of the AC side bridge; however, a variable frequency PWM with a defined phase shift is provided for leg 2. Due to the gating signal of leg 2, a quasi-square primary voltage having C2C phase shift w.r.t leg 1 gating signal, as well as secondary transformer voltage, appears as shown in Fig. 2.3. In method 1, the power flow can be regulated by varying the

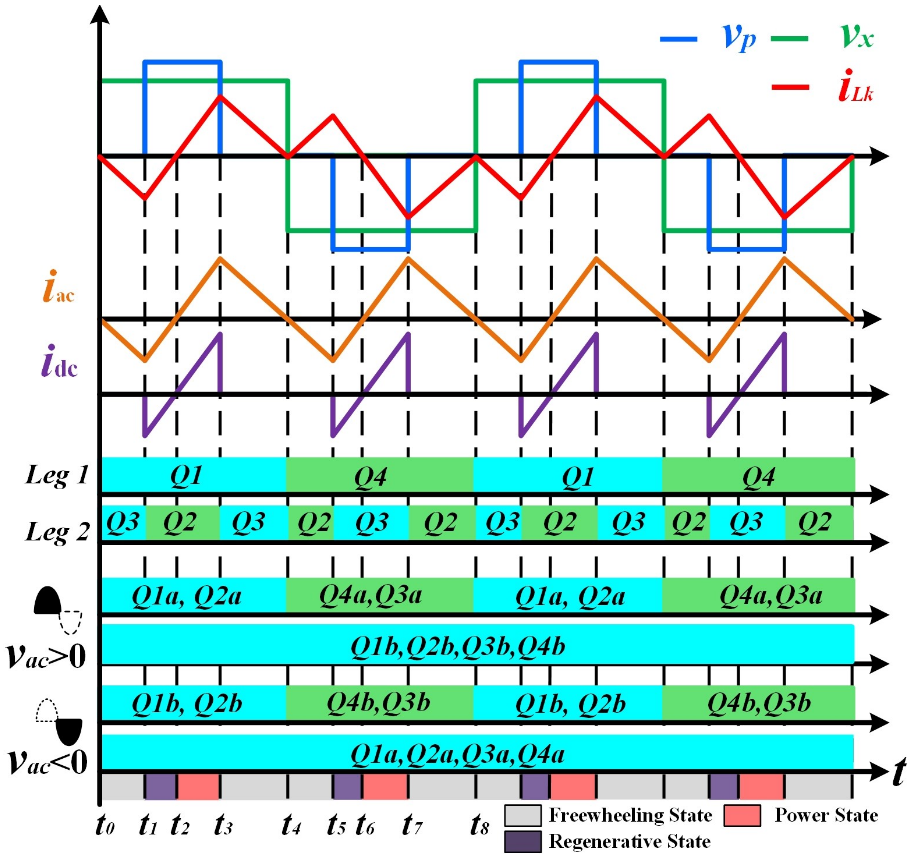

Figure 2.3: Switching sequence and principal operating waveform using method 1.

phase shift between the gating signal of leg 1 and leg 2. The switching operation of the converter is divided into three states as shown in Fig. 2.3, and these states further appear in various modes. These states are freewheeling states where i_{Lk} freewheels in the DC side H-bridge, regenerative states where power is delivered from sink to source, and power states where power is delivered from source to sink. Considering average power is flowing from the DC to AC side, various modes of operation are shown in Fig. 6 and discussed below for $i_{dc} > 0$ and $v_{ac} > 0$. It should be noted that the direction of all the currents is considered positive as given in the Fig. 2.1 and the body diodes are named after the switch, e.g., for switch $Q1a$, its body diode is named as $D1a$, and so on.

1) *Mode* 1 ($t_0 \leq t < t_1$): Fig. 2.4(a) shows the converter operating in mode 1. In this mode, the converter operates in a freewheeling state. At t=t_0, switches $Q1$, $Q3$ of the DC side bridge, and $Q1a$, $Q2a$ of the AC side bridge is provided with a gating

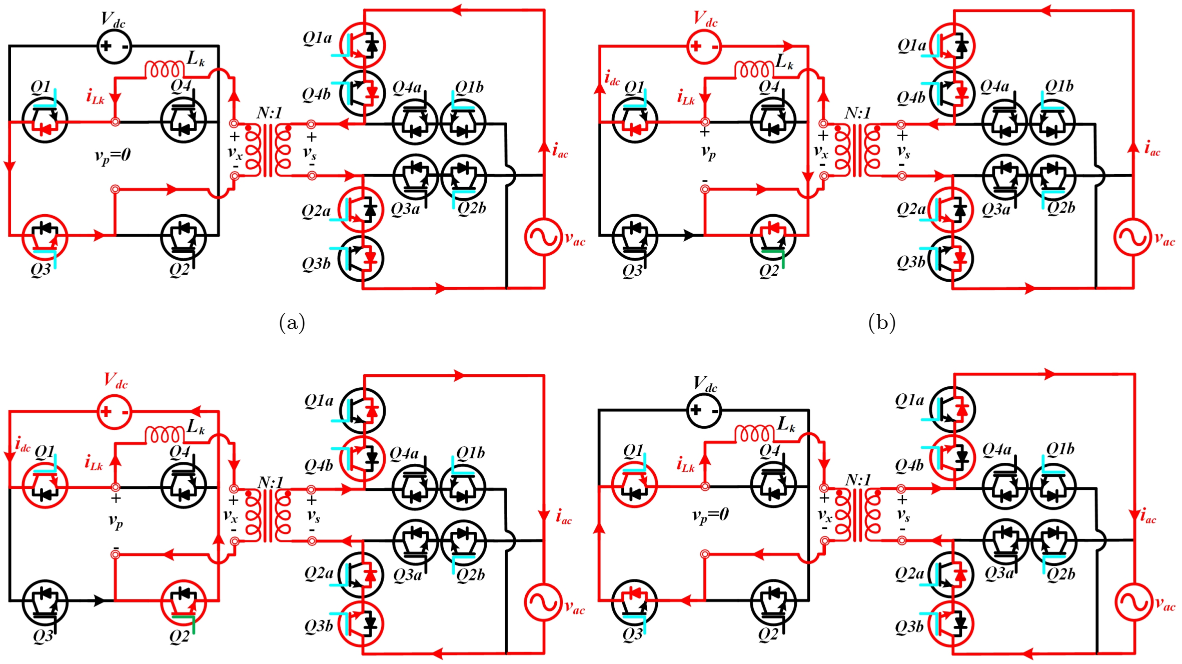

(a) (b)

(c) (d)

Figure 2.4: Various operating modes of the proposed modulation technique over half switching cycle of the converter using method 1 ($v_{ac} > 0$ and $i_{ac} > 0$). (a). Mode 1 ($t_0 \leq t < t_1$), (b). Mode 2 ($t_1 \leq t < t_2$), (c). Mode 3 ($t_2 \leq t < t_3$) and (d). Mode 4 ($t_3 \leq t < t_4$).

signal. At this switching instance $i_{Lk} = 0$, the primary side switches $D2$, $Q4$ turns OFF at ZCS, and $D1$, $Q3$ turn ON at ZCS. On the secondary side, $D3a$, $D4a$, $Q1b$, and $Q2b$ turn OFF at ZCS, and $Q1a$, $Q2a$, $D3b$, and $D4b$ turn ON at ZCS. v_{ac} appears across the secondary of the transformer (v_s=v_{ac}), a current Ni_{Lk} flow in the AC side from v_{ac} through $Q1a$, $D4b$, through secondary of the transformer, $Q2a$, $D3b$. A voltage induces in the primary of the transformer (v_x=Nv_{ac}) and due to this voltage, a freewheeling current i_{Lk} flow through the transformer primary, L_k, $D1$, $Q3$ results in $v_p = 0$. This mode 1 ends at $t = t_3$, during this mode current i_{dc}=0 and i_{ac}= i_{Lk}, and the span of this mode is $T_s(1 - m - \alpha)/4$.

2) *Mode* 2 ($t_1 \leq t < t_2$): Fig. 2.4(b) shows mode 2 operations of the converter in the regenerative state. At $t = t_1$, $Q3$ is turned OFF, $Q2$ is turned ON, V_{dc} appear before L_k (v_p=V_{dc}), and current commutates from $Q3$ to $D2$ in the primary. However, the

direction of i_{Lk} through L_k remains in the same direction as in mode 1. Current in DC side now flowing through transformer primary, L_k, $D1$, V_{dc}, and $D2$. In the secondary, Ni_{Lk} follows in the same way as in mode 1. Mode 2 ends at $t = t_2$, during this mode current $i_{dc}= i_{Lk}$ and $i_{ac}= i_{Lk}$ and the span of this mode is $mT_s(1 - m - \alpha)/4(1 - m)$.

3) *Mode* 3 ($t_2 \leq t < t_3$): The operation of the converter in power state is shown in Fig. 2.4(c). At $t = t_2$, direction of i_{Lk} changes and becomes positive. In this instance, the primary side switches $D1$, and $D2$ turn off at ZVS, and switch $Q1$, and $Q2$ turn ON at ZVS. Now i_{Lk} flows from V_{dc}, $Q1$, through L_k, transformer primary, and $Q2$ as shown in Fig. 2.4(c). On the secondary side, $Q1a$, $Q2a$ turn OFF at ZCS, $D3b$, and $D4b$ turn off at ZVS, and $Q3b$, $Q4b$, $D1a$, and $D2a$ turn ON at ZVS. Now, current Ni_{Lk} flows from the secondary of transformer $Q4b$, $D1a$, v_{ac}, $Q3b$, $D2a$, and supplies power to the load. Mode 3 ends at $t = t_3$, during this mode current $i_{dc}= i_{Lk}$ and $i_{ac}= i_{Lk}$, and the span of this mode is $mT_s(1 - m + \alpha)/4(1 - m)$.

4) *Mode* 4 ($t_3 \leq t < t_4$): The operation of the converter in a freewheeling state is shown in Fig. 2.4(d). At $t = t_3$, $Q2$ is turned OFF and $Q3$ is turned ON. Now, i_{Lk} commutates from the switch $Q2$ to $D3$. Current i_{Lk} freewheels through the primary of the transformer, $D3$, $Q1$, and L_k resulting in $v_p = 0$. In the secondary of the transformer, Ni_{Lk} flows in the same direction as in mode 3. Mode 4 ends at $t = t_4$, during this mode current $i_{dc}= 0$ and $i_{ac}= i_{Lk}$, and the span of this mode is $T_s(1 - m + \alpha)/4$. Converter operating in the second half-time period ($t_4 < t < t_8$) in the same manner as in the first half-time period. In the second half-time period $Q4a$, and $Q3a$ participate in the switching instead of $Q1a$ and $Q2a$. The status of the switches at various switching instances is shown in Table 2.2 for $v_{ac} > 0$.

2.2.3 Modulation Technique Using Method 2

Fig. 2.5 shows the switching sequence and principal waveform using method 2. The gating signal for leg 1 is now phase-shifted compared to the AC side bridge. However, a

Table 2.2: Status of the Switches During Transition In DC to AC Power Flow Using Method 1.

Instances	Status of the Power Switches
t_0	$D1, Q3, Q1a, Q2a, D3b, D4b$ ZCS Turn ON; $D2, Q4, D3a, D4a, Q1b, Q2b$ ZCS Turn OFF;
t_2	$Q1, Q2, D1a, D2a, Q3b, Q4b$ ZVS Turn ON; $D1, D2, D3b, D4b$ ZVS Turn OFF; $Q1a, Q2a$ ZCS Turn OFF;
t_4	$Q2, D4, Q3a, Q4a, D1b, D2b$ ZCS Turn ON; $Q1, D3, D1a, D2a, Q3b, Q4b$ ZCS Turn OFF;
t_6	$Q3, Q4, D3a, D4a, Q1b, Q2b$ ZVS Turn ON; $D3, D4, D1b, D2b$ ZVS Turn OFF; $Q3a, Q4a$ ZCS Turn OFF;

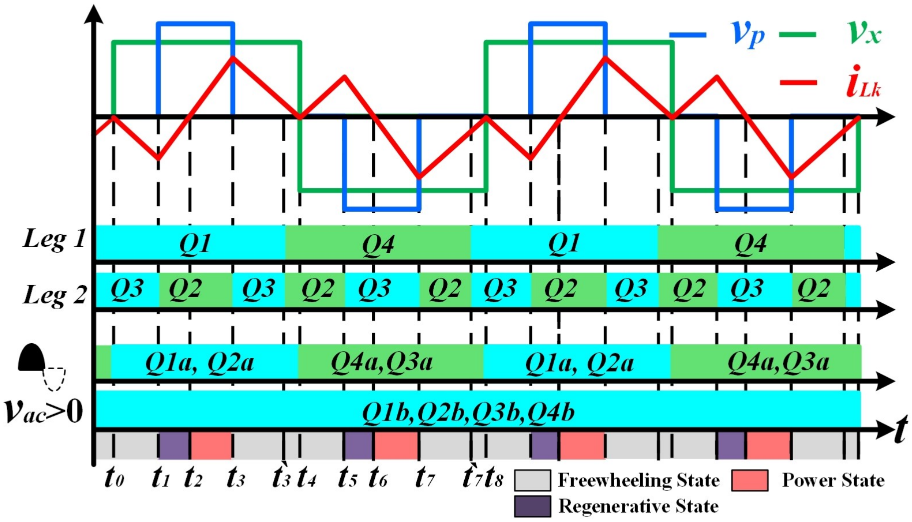

Figure 2.5: Switching sequence and principal operating waveform using method 2.

variable frequency PWM resulting in the quasi-square primary voltage has zero phase w.r.t the gating signal of leg 1 ($Q1$ and $Q2$ center is aligned) as seen in Fig. 2.5. In this method, the power flow is due to the phase shift between the gating signal of leg 1 and the AC side bridge. Various modes over half-time period of the converter are shown in Fig. 2.6 (a)-(e). One extra mode i.e., mode 5 from t_3' to t_4 has been introduced. Mode 1 to Mode 4 is the same as that of Method 1, however, Mode 5 is necessary to discuss.

1) *Mode* 5 ($t_3' \leq t < t_4$): Fig. 2.6(e) shows the converter operating in a freewheeling

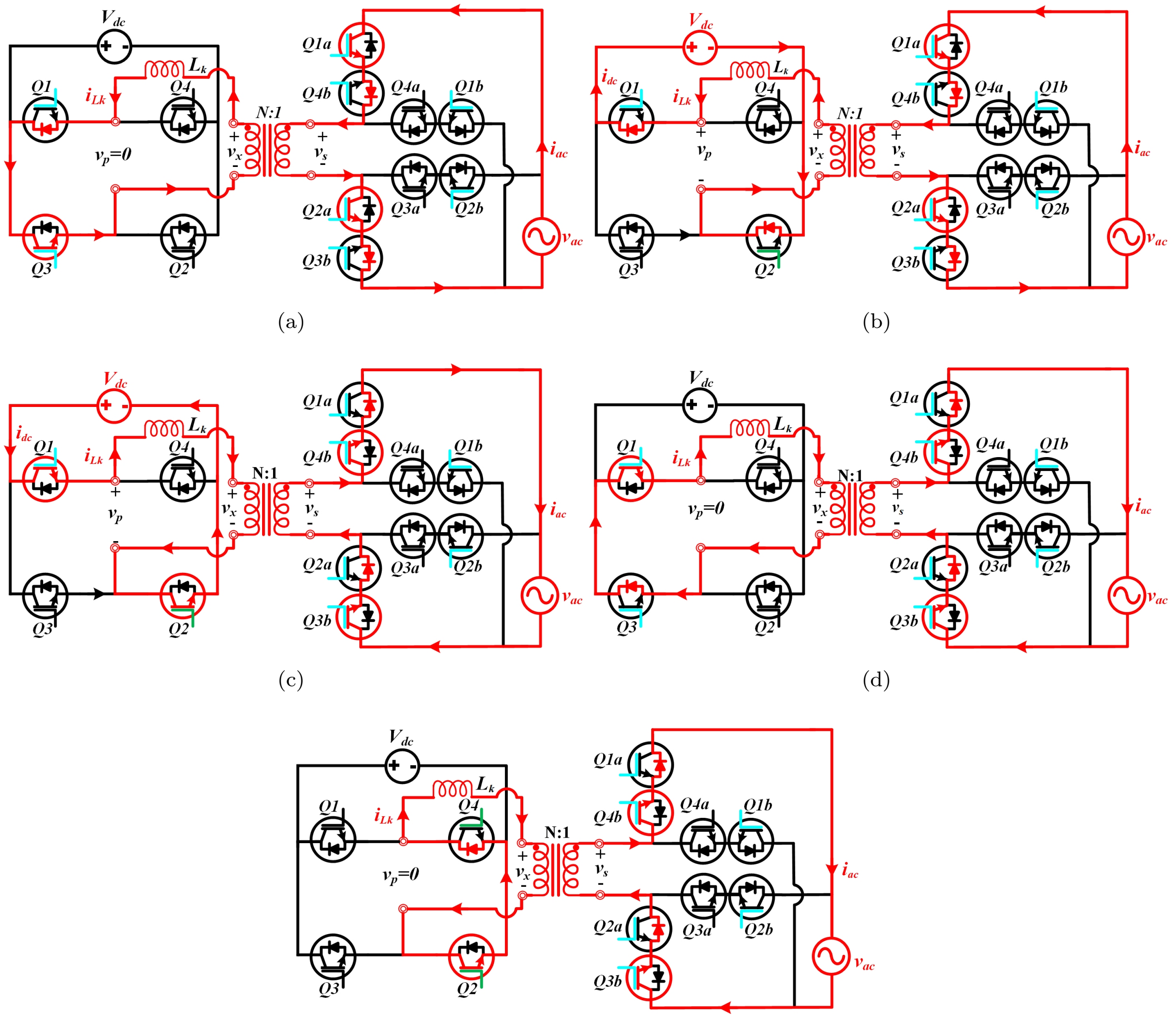

(a) (b) (c) (d) (e)

Figure 2.6: Various operating modes of the proposed modulation technique over half switching cycle of the converter using method 2 ($v_{ac} > 0$ and $i_{ac} > 0$). (a). Mode 1 ($t_0 \leq t < t_1$), (b). Mode 2 ($t_1 \leq t < t_2$), (c). Mode 3 ($t_2 \leq t < t_3$) and (d). Mode 4 ($t_3 \leq t < t_3{'}$) (e). Mode 5 ($t_3{'} \leq t < t_4$).

state. At $t = t_3{'}$, $Q1$ and $Q3$ are turned OFF, and $Q4$ and $Q2$ are turned ON which results in current i_{Lk} commutating from $Q1$ to $Q2$ and $D3$ to $D4$ of the DC side bridge. Now current flows through L_k, transformer primary, $Q2$, and $D4$. In the secondary side Ni_{Lk} flow through transformer secondary, $Q4b$, $D1a$, v_{ac}, $Q3b$, and $D2a$. Mode 5 ends at $t = t_4$,, during this mode current $i_{dc} = 0$ and $i_{ac} = i_{Lk}$ and the span of this mode is $\alpha T_s/4$. Table 2.3 shows the status of the power switches using modulation technique 2.

Table 2.3: Status of the Switches During Transition in DC to AC Power Flow Using Method 2.

Instances	Status of the Power Switches
t_0	$Q1a, Q2a, D3b, D4b$ ZCS Turn ON; $D3a, D4a, Q1b, Q2b$ ZCS Turn OFF;
t_2	$Q1, Q2, D1a, D2a, Q3b, Q4b$ ZVS Turn ON; $D1, D2, D3b, D4b$ ZVS Turn OFF; $Q1a, Q2a$ ZCS Turn OFF;
t_4	$Q3a, Q4a, D1b, D2b$ ZCS Turn ON; $D1a, D2a, Q3b, Q4b$ ZCS Turn OFF;
t_6	$Q3, Q4, D3a, D4a, Q1b, Q2b$ ZVS Turn ON; $D3, D4, D1b, D2b$ ZVS Turn OFF; $Q3a, Q4a$ ZCS Turn OFF;

2.3 DSP Based Digital Realization of Proposed Techniques

2.3.1 Digital Realization of Method 1

This section presents the DSP-based digital realization of method 1, showcasing simplicity through the utilization of a single carrier/counter using TMDSDOCK28335. Method 1 can be realized using a distinctive single Up-Down counter/carrier having a time-base period register (TBPRD) value assigned as one-quarter of the switching time period in the digital domain. To generate various PWMs for the switches, two counter-compare registers are required, namely the counter-compare A register (CMPA) and counter-compare B register (CMPB), as shown in Fig. 2.7. PWM signals for the Leg 1 and AC side bridge can be generated using CMPA only, whose value is assigned as TBPRD-|PHS| where PHS is the phase value equivalent to Δt in the digital domain. The gating signal for the leg 1 and AC side bridge can be generated using the toggle ($\updownarrow$) command, each time when CMPA equals the down slope of the Up-Down counter as shown in Fig. 2.7. To generate variable frequency PWM, CMPA and CMPB are needed. CMPB equals V_{ref} in the digital domain. When CMPA equals the Down slope and CMPB equals both Up and Down slope, then the toggle is initiated, resulting in the PWM

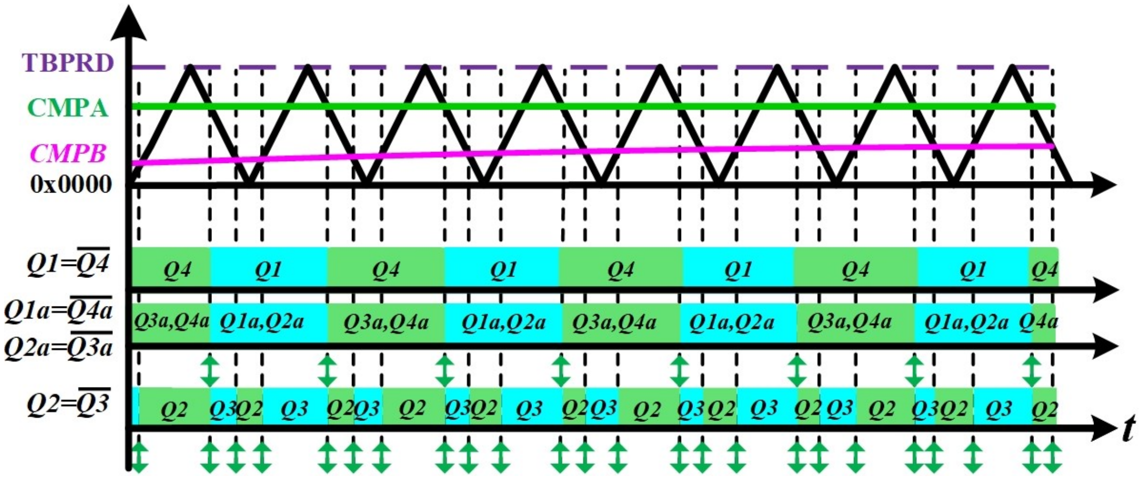

Figure 2.7: DSP-based digital realization of method 1 and gating signals of various switches.

for Leg 2. PWM signals generated from each enhanced PWM module of F28335 are complementary to each other and can be programmed to stay ON for half a cycle of line frequency by operating the trip zone in cycle-by-cycle mode. Fig. 2.8 illustrates the correlation between the ON time of the DC side diagonal switches and the C2C phase, showcasing PWMs for bidirectional power flow for half time period. In Fig. 2.8, two carriers have been shown for each case. In Fig. 2.8 (a), when power flows from DC to AC side, and in Fig. 2.8(b), when power flows from AC to DC side. The dotted counter (····) is the projection of two Up-Down counters with a phase shift of Δt, considering from the vertex of the Up slope of one and the Down slope of the other counter. The difference between the TBPRD of these two counter projections with and without phase shift is Δt. The switching sequence and width of various sections are shown in Fig. 2.8 to visualize digital domain realization using any DSP.

2.3.2 Digital Realization of Method 2

In method 2 shown in Fig. 2.9, to generate PWM for leg 1, again the toggle command is utilized when the time-based counter reaches the active period (CTR=PRD) of the Up-Down counter. As a result, no counter-compare register is required for the leg 1

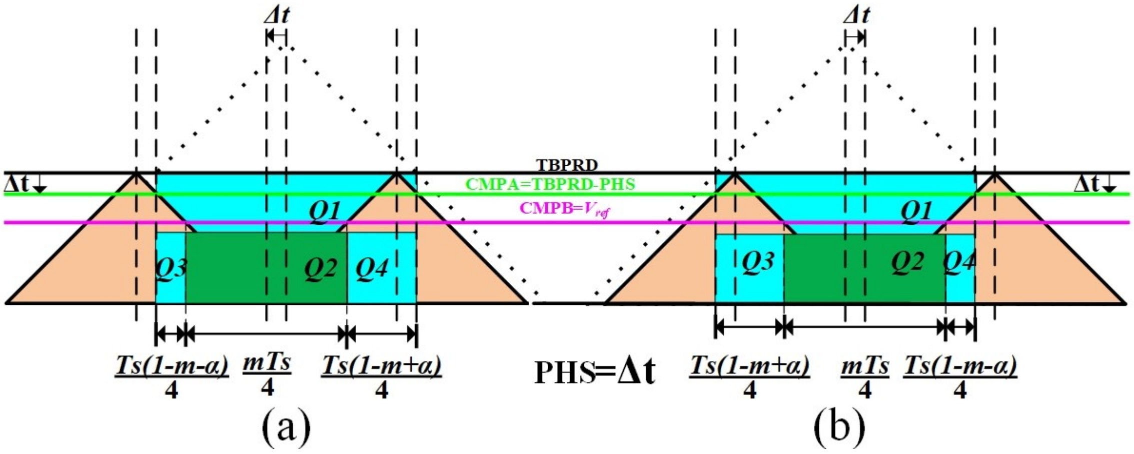

Figure 2.8: Pictorial representation of DSP-based digital realization bidirectional power flow using proposed modulation technique using method 1. (a) DC to AC power Flow and (b) AC to DC power flow.

gating signal. To generate an AC side bridge gating signal, CMPA is defined to be TBPRD-|PHS| and toggled when it equals the Down slope of the Up-Down counter. Variable frequency PWM for leg 2 can be generated using PRD of the Up-Down counter and CMPB (CMPB=V_{ref}). Again, the toggling command is used at the PRD, and when CMPB equals Up slope and Down slope of the Up-Down counter. Digital realization and generation of the gating signal for DC to AC power flow using method 2 can be seen in Fig. 2.9.

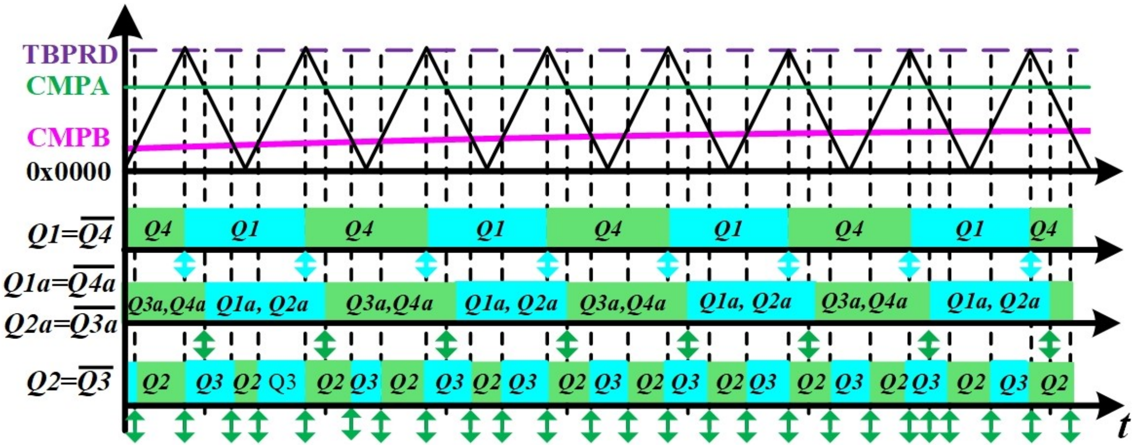

Figure 2.9: DSP-based digital realization of method 2 and gating signals of various switches.

2.4 Simulation and Experimental Validation

2.4.1 Simulation Validation

The topology shown in Fig. 2.1 has been simulated in the PSIM software using the parameters presented in the Table. 2.4 at 500 W using method 1. Fig. 2.10 (a)-(d) shows the converter transferring power from the DC to AC side (V2H mode). Fig. 2.10(a) shows the gating pulses when the instantaneous AC voltage reaches its peak. The C2C phase shift of 27° between the gating signal of $Q1$ and $Q2$ is provided. The $Q1$ is operated at 50% of the duty, whereas the $Q2$ and $Q3$ are operating at variable frequencies and are complementary to each other. Fig. 2.10(b) shows the input voltage (V_{dc}), input current (I_{dc}), output voltage (v_{ac}) and output current (i_{ac}) over five cycles of the line frequency. It can be observed in Fig. 2.10(b) that line voltage and current are in the same phase and have a power factor close to unity. The RMS value of the i_{ac} is 8.66A, and the average value of the I_{dc} is found to be 3.9A and has a fundamental frequency of 100 Hz. Fig. 2.10(c) shows the nature of various transformer voltages and current waveforms. The zoomed view of Fig. 2.10(c) close to the instantaneous peak value of v_{ac} is shown in Fig. 2.10(d). In Fig. 2.10(d), the quasi-square primary voltage of the transformer (v_p) whose peak value is equal to the magnitude of the V_{dc} and secondary voltage (v_s) of the transformer whose peak value is the same as the instantaneous value of v_{ac}. The corresponding current through the leakage inductance is shown in Fig. 2.10(d). It can be observed from the figure that $i_{Lk}(t_0)$ and $i_{Lk}(t_4)$ are zero, resulting in the ZCS for converter switches. The magnitude of the peak leakage current occurring at t_3 and t_7 instances is found to be $\approx$ 27.4A.

Similarly, Fig. 2.10 (e)-(f) shows the converter transferring power from AC to DC side (G2V mode). To emulate this mode, the converter is simulated using $\alpha = -27°$ to ensure the power transfer from the AC to the DC side. Various input and output voltages are shown in Fig. 2.10(e). The average I_{dc} is found to be -3.81A. Since the

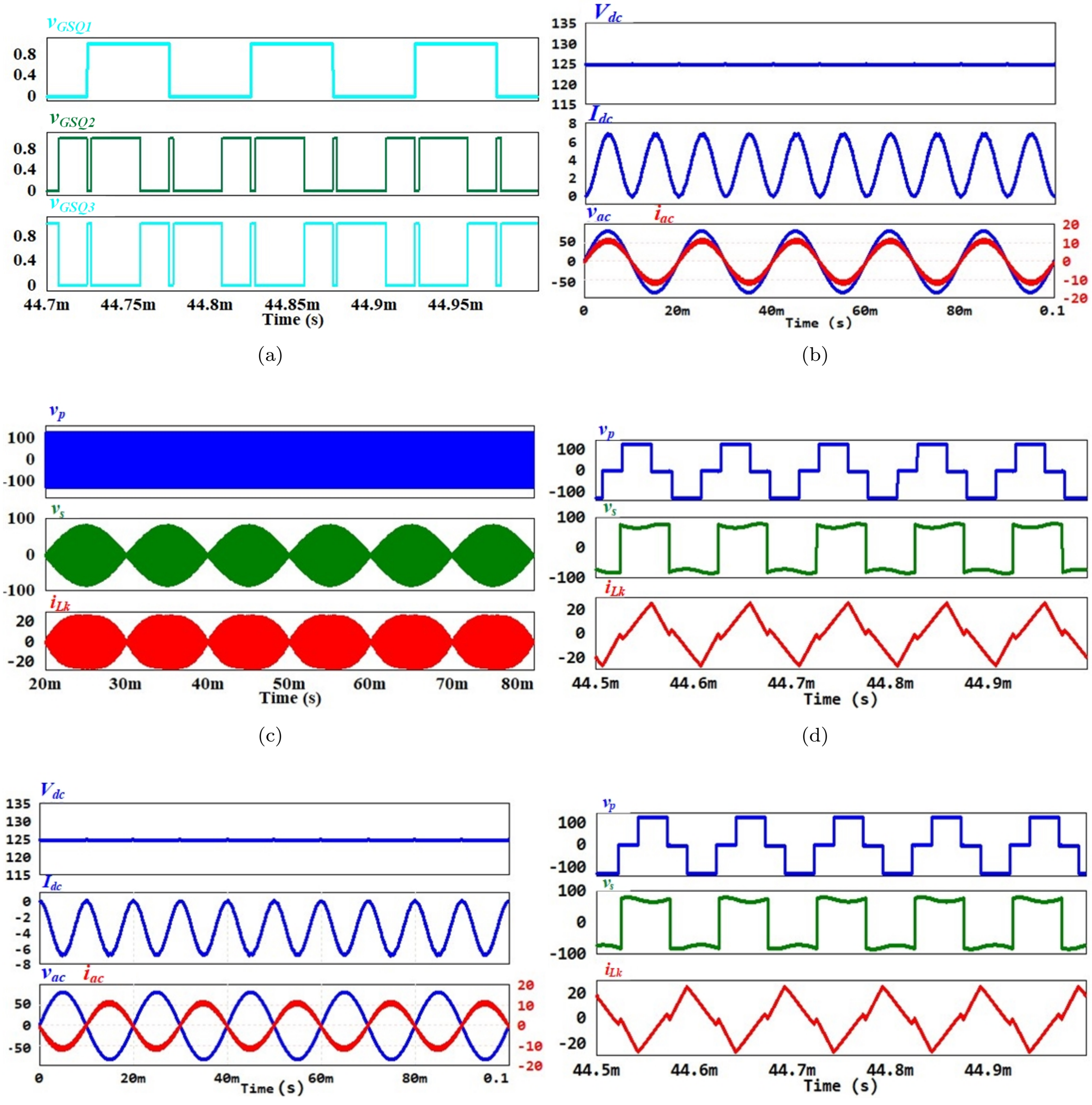

(a) (b)

(c) (d)

(e) (f)

Figure 2.10: Simulation results using method 1; (a) Gating pulses to the primary bridge. (b) Input, output voltages, and currents for DC-AC power flow. (c) Transformer voltages and currents. (d) Zoomed view of Fig. 12(c). (e) Input, output voltages, and currents for AC-DC power flow. (e) Zoomed view of transformer voltages and current for DC-AC power flow.

direction of the current is considered positive for DC to AC power flow, the I_{dc} is negative, and i_{ac} is 180° out of phase w.r.t AC voltage as shown in Fig. 2.10(e). Fig. 2.10(f) shows the v_p, v_s and i_{Lk} for 5 switching cycles. The v_p is now lagging w.r.t v_s by

Table 2.4: Design Parameters

Parameters	**Selected Values**
Input DC voltage (V_{dc})	$125V$
Output AC voltage (v_{ac})	$75sin(2\pi ft)$
Leakage inductance (L_k)	$54\mu H$
Switching Frequency (f_s)	$10kHz$
N	1
Δt	$8.8\mu s$

27° and operating in the G2V mode. The current i_{Lk} is now out of phase as compared with the V2H operation. Simulation results using the proposed modulation technique are further validated using parameters shown in Table 2.4 in the next subsection.

2.4.2 Experimental Validation

A scale-down experimental prototype of 500W shown in Fig. 2.11 has been developed to verify method 1. Design parameters and component specifications selected for the prototype development are listed in Table 2.4 and 2.5. Leg 2 of DC side bridge consists of a pair of IXFH120N30X3 MOSFETs, and the rest of the switches consist of a pair of IKW30N65ET7 IGBTs. The DC side filter consists of an inductance of $104m$H and a capacitance of 100μF. The transformer consists of 25 turns on both sides with the magnetizing inductance of $3.76m$H and leakage inductance of 54μH. An inductance of 100μH and a capacitance of 50μF are selected for the AC side filter. Proposed switching sequences are generated using TI based TMS320F28335 controller and MATLAB-integrated embedded coder support package for TI C2000 processors. The LV25-P voltage sensor is used for sensing both voltages. The trip zone operated in cycle-by-cycle mode ensures the enable high for Qxa (x=1,2,3,4) for a negative half cycle of line voltage and vice versa for Qxb switches.

Fig. 2.12 (a)-(g) shows various experimental waveforms during V2H power flow. Fig. 2.12(a) shows the PWM signals for the diagonal switches $Q1$, $Q2$ of the DC side

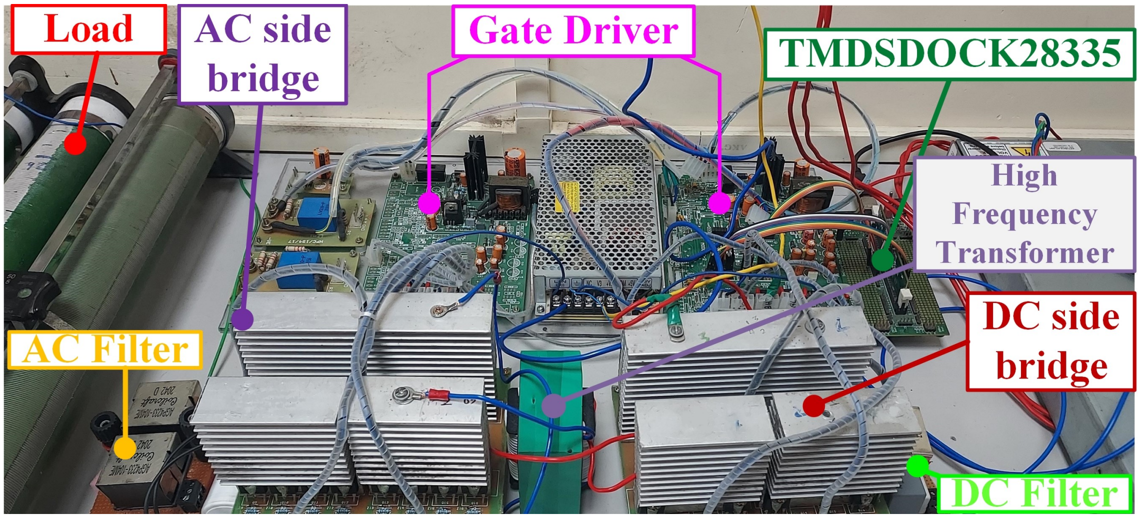

Figure 2.11: Experimental prototype of single-phase single-stage bidirectional DC to AC dual active bridge converter.

Table 2.5: Component Selected

Component	**Name/Make/Model**
Switches	IKW30N65ET7, IXFH120N30X3
DSP Controller	TMS320F28335
Gate Driver Optocoupler	FOD3184 and A3120
Voltage Sensor	LV25-P
Transformer Core	EE8040 CF139
AC Filter Capacitor	ARCOS 50μF
AC Filter Inductor	PCV-2-104-10L
DC Filter Capacitor	KEMET 47μF
DC Filter Inductor	AGP4233 104ME

bridge, and $Q1b$, $Q2a$ of the AC side bridge captured before the gate driver. Fig. 2.12(b) shows a zoomed view of Fig. 2.12 (a) when the line voltage reverses its polarity. From Fig. 2.12(b), it can be observed from the waveform of the V_{Q2GS} that the intermediate pulse width increases exponentially before and after the zero crossing of the line voltage, resulting in an increasing width of the variable frequency PWM signal. Fig. 2.12(c)

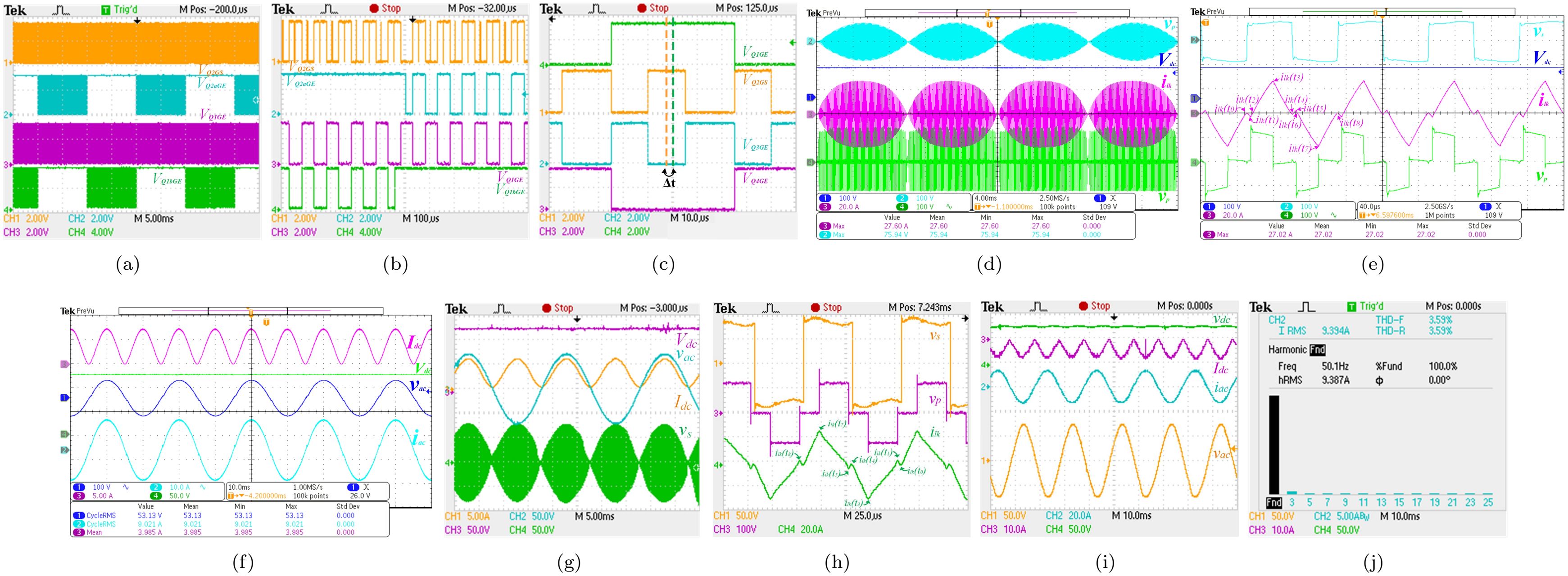

(a) (b) (c) (d) (e)

(f) (g) (h) (i) (j)

Figure 2.12: Experimental results showing (a) Gate pulses for the various switches. (b) Zoomed view of the (a) near zero crossing of v_{ac}. (c) Gate pulses for the DC side bridges when power is delivered from the DC to the AC side. (d) Showing V_{dc}, v_p, v_s, and i_{Lk}, for two cycles of line frequency. (e) Zoomed view of Fig. 14(d). (f) Showing v_{ac}, i_{ac}, I_{dc} and V_{dc}. (g) Showing i_{ac}, v_{ac}, V_{dc}, and v_s for AC to DC power flow. (h) Showing v_s, v_p, and i_{Lk} when power is delivered from AC to DC side. (i) Showing input v_{ac}, i_{ac}, I_{dc} and V_{dc}. (j) THD of i_{ac} during AC to DC power flow.

shows the gate pulses of $Q1$ and $Q2$. V_{Q2GS} is in phase lead with respect to V_{Q1GE} when perceived from C2C during ON time. As a result of this switching, C2C phase-shifted voltages w.r.t each other appear across the transformer. Fig. 2.12(d) shows i_{Lk}, v_p, V_{dc}, and v_s for two cycles of the line frequency. The nature of the experimental and simulation results shown in Fig. 2.12(d) and Fig. 2.10(c) complement each other. A zoomed view of Fig. 2.12(d) close to the peak value of the instantaneous AC voltage is shown in Fig. 2.12(e). The current i_{Lk} at the various instances is shown in Fig. 2.12(e). In this figure, i_{Lk} at t_0, t_2, t_6, and t_8 is zero, which results in soft switching turn ON and OFF in AC side bridge and DC side bridge as described in Table 2.3. At this switching instance, the peak value of the v_s is 125V, v_p is 75V and i_{Lk} is $\approx$ 27A ($|i_{Lk}(t_3)| = |i_{Lk}(t_7)|$). The nature of i_{Lk} is due to the proposed modulation technique, resulting in the true ZCS in the AC side switches, which results in reduced switching loss at higher instantaneous v_{ac}. Fig. 2.12(f) shows output voltages and currents where V_{dc}, I_{dc}, v_{ac}, and i_{ac} found to be 125 V, 3.98 A, 53.13 V and 9.02 A. The AC voltage and current are in the same phase, resulting in a near unity power factor. Fig. 2.12(g) shows V_{dc}, I_{dc}, v_{ac} with transformer secondary voltage v_s.

To emulate G2V, a setup for AC to DC power flow is made by connecting Ametek AST1501 as a source and Maynuo M9715B DC electronic load connected at the DC side. The α is now selected negative to make sure the diagonal switches of leg 2 lag behind leg 1 during ON time. Also, the toggle sequence for AC to DC power flow is now reversed as presented in Fig. 2.8(b). Experimental validation for the AC to DC power flow is shown in Fig. 2.12(h)-(i). In Fig. 2.12(h), v_s, v_p and i_{Lk} is shown. The peak value of the v_s is 125V, v_p is 75V and i_{Lk} is $\approx$ 27.7A ($|i_{Lk}(t_3)| = |i_{Lk}(t_7)|$). Fig. 2.12(i) shows the v_{ac}, i_{ac}, I_{dc}, and V_{dc}. Current i_{ac} is now out of phase compared with v_{ac} therefore, the power is now delivered from AC to DC side and I_{dc} is now negative which is equal to 3.65A and RMS value of the $i_{ac}$is now 9.4 A. The Total harmonic distortion (THD) of the grid current is found to be 3.59% as shown in Fig. 2.12(j).

2.5 Discussion

2.5.1 Dynamic Performance

Fig. 2.13(a) shows the dynamic performance of the matrix-type DAB for ≈ 51% step change in the load from 500W to 248W using method 1. Before dynamics, the converter was operating at constant voltage mode and drawing an RMS current of 10.54A. After dynamics, v_{ac} settles within three cycles of the AC and now draws an RMS current of 5.23A. Fig. 2.13(b) shows the transformer voltages and current before dynamics. The

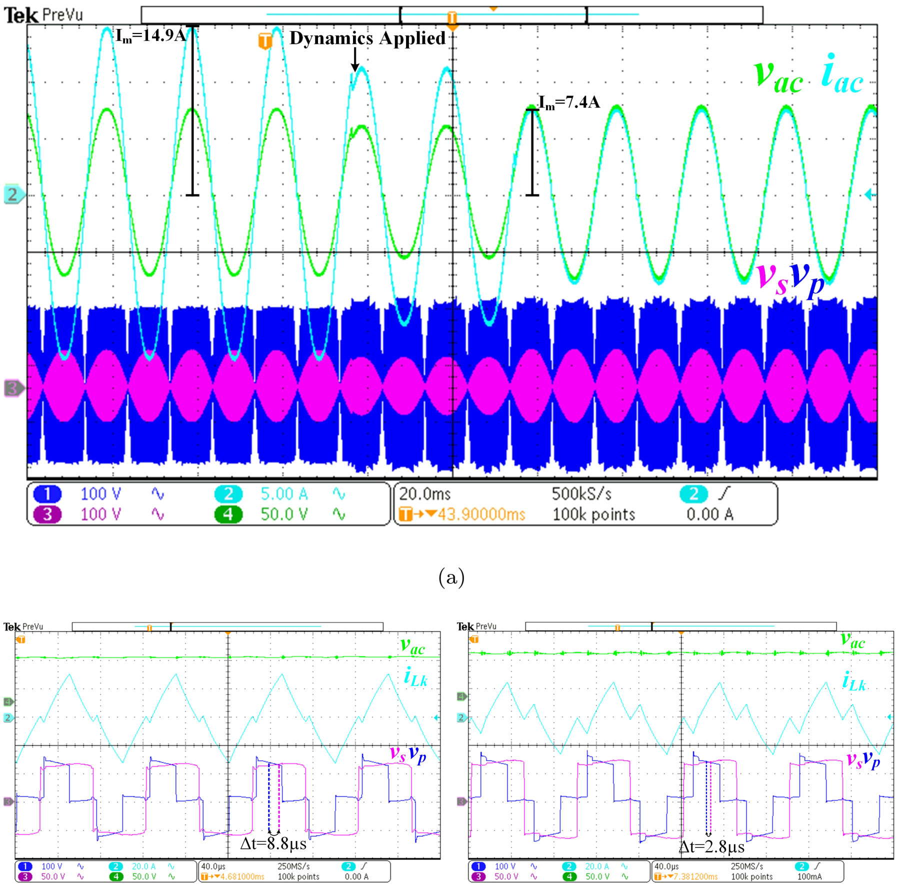

(a)

(b)

(c)

Figure 2.13: Dynamic performance under 51% step change in the load. (a) Showing dynamics variation from 500 W to 248 W. (b) Showing transformer voltages and current before dynamics. (c) Showing transformer voltages and current after dynamics.

C2C phase shift of 8.8μs is present between v_s and v_p before dynamics. After dynamics, the new C2C phase shift between v_s and v_p becomes 2.8μs as shown in Fig. 2.13(c). The soft switching operation of the converter before and after dynamics remains intact using the proposed modulation technique, which can be observed in Fig. 2.13(b) and Fig. 2.13(c).

2.5.2 Soft Switching Analysis

In Fig. 2.14(a) and Fig. 2.14(b), before time t_2, gating signal of $Q1$ (v_{Q1GE}) was high, i_{Lk} was negative and flowing through $D1$ and $D2$ resulting in voltage across collector emitter (v_{Q1CE}) was zero. For instance, t_1, i_{Lk} become positive, and $Q1$ starts conducting, resulting in zero voltage turn ON of $Q1$. In Fig. 2.14(c) and Fig. 2.14(d), before time t_4, v_{Q1GE} was present, v_{Q1CE} was zero because $Q1$ and $D3$ was conducting and i_{Lk} was positive. When i_{Lk} reaches zero at t_4, v_{Q1GE} removed and $Q1$ turn OFF at zero current. In Fig. 2.14(e) and Fig. 2.14(f), before time t_0, gating signal of $Q3$ (v_{Q3GS}) was absent, voltage across collector emitter (v_{Q3DS}) was same as instantaneous input voltage. Current i_{Lk} was negative and flowing through $Q4$ and $D2$. At t_0, i_{Lk} reaches zero, v_{Q3GS} is applied resulting in v_{Q3DS} becoming zero, and then $Q3$ start conducting resulting in zero current turns ON of $Q3$. In Fig. 2.14(g) and Fig. 2.14(h), before t_4, $Q1$ and $D3$ was conducting and i_{Lk} is positive. Once i_{Lk} reaches zero at t_4, the v_{Q3GS} is removed, $Q3$ turn OFF at zero current. Before t_6, i_{Lk} is positive and flowing through $D3$ and $D4$. At t_6, i_{Lk} becomes negative and $D3$ starts conducting, resulting in a zero voltage turn of $Q3$.

Fig. 2.14(i) and Fig. 2.14(j) showing simulation and experimental results of ZCS turn ON of $Q1a$. For $v_{ac} > 0$, before t_0, gating signal of $Q1a$ (v_{Q1aGE}) was absent and $Q1a$ was OFF, voltage across collector emitter (v_{Q1aCE}) was same as instantaneous v_{ac}, i_{Lk} was negative and flowing through the diode $D3a$, $D4a$. When i_{Lk} reaches zero, v_{Q1aGE} is applied and v_{Q1aCE} becomes zero. Now i_{Lk} flowing through $Q1a$ and $Q1a$

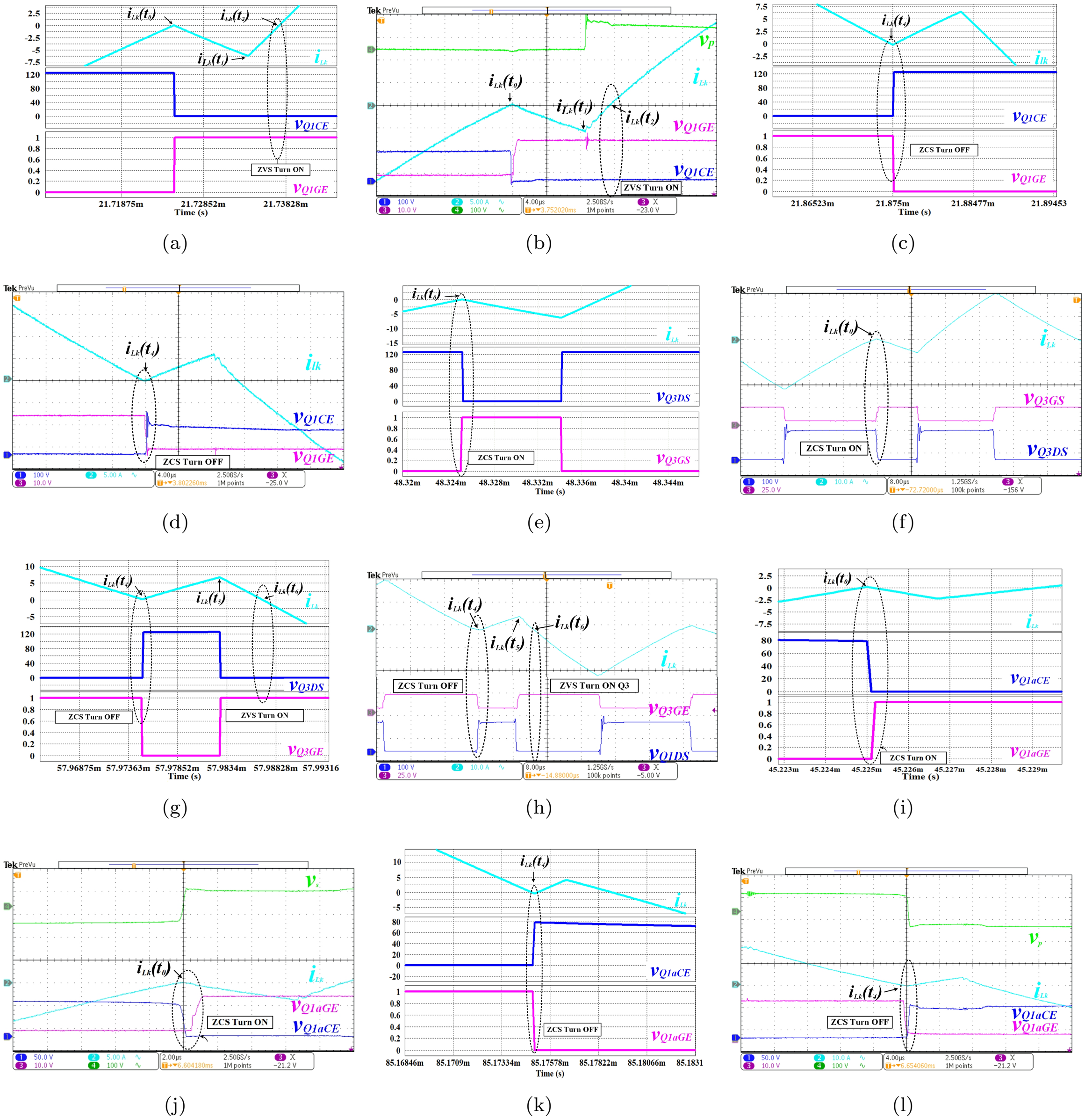

(a) (b) (c)

(d) (e) (f)

(g) (h) (i)

(j) (k) (l)

Figure 2.14: Simulation and experimental results of soft switching. (a) simulation and (b) experimental results of ZVS turn ON of DC side switch $Q1$. (c) simulation and (d) experimental results of ZCS turn OFF of DC side switch $Q1$. (e) simulation and (f) experimental results of ZCS turn ON of DC side switch $Q3$. (g) simulation and (h) experimental results of ZCS turn OFF and ZVS Turn ON of DC side switch $Q3$. (i) simulation and (j) experimental results of ZCS turn ON of AC side switch $Q1a$. (k) simulation and (l) experimental results of ZCS turn OFF of AC side switch $Q1a$.

turn ON at zero current. In Fig. 2.14(k) and Fig. 2.14(l) before t_4, v_{Q1aGE} was present, v_{Q1aCE} was zero because i_{Lk} was positive and flowing through $D1a$ and $D2a$. At t_4,

i_{Lk} reaches zero, v_{Q1GE} is removed, resulting in $Q1a$ turning OFF at zero current, and v_{Q1CE} becomes the same as the instantaneous output AC voltage.

2.5.3 Comparison of the Proposed Method with the Existing Literature

In Table 2.6, a comparative analysis of the presented technique with existing literature is shown. A variable frequency and EPS modulation are presented, having three DoF [110]. This technique offers bidirectional power flow with ZVS ON for all switches and realization done using FPGA FPGA-based controller. The variable frequency with the phase shift modulation technique is difficult to realize due to the optimization algorithm involved in evaluating DoF [110]. A DSP+FPGA-based triple-phase shift controlled bidirectional resonant AC to DC DAB offering ZVS ON for all switches is presented in [136]. The technique has 5 modes of operation and has a nonlinear relationship between its electrical parameters and control variables[136]. A DSP+FPGA-based unipolar PWM technique is presented, which offers ZVS or ZCS for DC side switches and ZCS for AC side switches [54]. AC to DC power flow having 4 modes and AC to DC power flow having 8 modes are presented in the paper. Two modulation techniques using dual carrier unipolar sinusoidal PWM-based technique are presented using DSP [64]. There are 8 modes for non-synchronous and 10 modes for synchronous-based modulation techniques, which is realized using DSP. Bidirectional power flow is not possible using any of the presented techniques [64]. A unipolar sinusoidal PWM-based bidirectional AC to DC DAB offers ZVS ON for DC switches and ZVS for AC side switches presented in [65]. This converter has 10 modes for DC to AC power flow, and 6 modes for AC to DC power flow are realized using DSP. A double carrier-based DC to AC dual active bridge offering ZVS for DC switches and ZCS for AC switches is realized using a DSP + FPGA-based controller having 5 modes of operation presented in [68]. A reduced switch count, double carrier-based DC to AC DAB using FPGA is presented in [151]. The presented technique has 5 modes and offers ZVS for all switches. A simulation-based double carrier unidirectional AC to DC DAB offering ZCS ON for the AC side switches has been presented [66]. There are 5 modes of operation over half the switching cycle of the converters, resulting in hard switching on the DC side [66].

In this chapter, a variable frequency and single-phase shift modulation technique has been proposed that can be realized using two methods. In comparison with techniques present in Table 2.6, the proposed technique offers bidirectional power flow, and linear control due to the presence of a single variable and offers ZVS turn ON, ZCS turn OFF for DC side switches, ZCS turn ON and OFF for all the switches of AC side bridge. Method 1 has 4 modes, and Method 2 has 5 modes of operation. Four switches of the AC side bridge operate for half a cycle of the line frequency, and both methods can be realized using a single carrier, having a limited number of switching modes. In comparison [54, 68, 136], the proposed method does not require any multiprocessor MCU for its realization. Furthermore, despite employing variable frequency operation, its realization does not require complex mathematical evaluations or optimization techniques to realize, as compared with [110].

2.5.4 Efficiency Comparisons with Other TRM

Table 2.7 shows the comparison between the proposed TRM with the other existing TRMs. An FPGA-based MCU with a half-bridge configuration is used to realize the modulation in [44]. However, the technique requires multiple mathematical computations, involving two different shapes and frequency waves, which makes its realization moderately difficult. A DSP-based MCU with full bridge configuration uses TPS and has at least four modes of operation over a half cycle of AC presented in [114]. However, the technique calculates online global optimal working modes, three DoF, which makes it moderately complex to realize. Furthermore, these modulation techniques have higher THD at lower operating wattage. A TRM based on single H-bridge modulation is proposed for single-phase [120] and three-phase [146] converters. The modulation

Table 2.6: Comparison with Various Modulation Techniques

Criteria		[54]	[64]	[65]	[66]	[68]	[110]	[136]	[151]	Proposed
Method of Modulation Technique		Unipolar+ PWM	Unipolar Sinusoidal PWM	Unipolar Sinusoidal PWM	PWM	PWM	Variable Frequency Extended Phase Shift	Triple-Phase Shift	PWM+ Phase Shift	Variable Frequency and Single-Phase Shift
Power Flow Direction Presented		Bidirectional	DC to AC	Bidirectional	AC to DC	DC to AC	Bidirectional	Bidirectional	DC to AC	Bidirectional
Switch Status	**DC Side**	ZVS or ZCS	ZVS	ZVS ON	Hard Switch	ZVS	ZVS ON	ZVS ON	ZVS	ZVS ON ZCS OFF
	AC Side	ZCS	ZCS	ZVS	ZCS	ZCS	ZVS ON	ZVS ON	ZVS	ZCS
Number of Switches (S+D)#		24	24	24	24	24	12*	24*	16	24
Number of Carrier		1	1	1	2	2	Not Reported	Not Reported	2	1
No. of Modes Over Half Switching Cycle		DC to AC-4 AC to DC-8	8,10 (two)	DC to AC-10 AC to DC-6	5	5	4	5	5	4, 5
No. of Power Switches Operating at Line Frequency		2	2	4	0	0	2	4	0	4
Controller Used for Realization		DSP+FPGA	DSP	DSP	NA	DSP+FPGA	FPGA	DSP+FPGA	FPGA	DSP
Efficiency		Not Reported	96%	96.25%	Not Reported	Not Reported	95%	94.5%	91.1%	96.19%

#(S+D)= Switches and diode. Body diode is also considered a separate entity

*AC side bridge is a half bridge

Table 2.7: Efficiency comparison with the proposed and existing TRM

Papers	Maximum Efficiency (η)	Power at Maximum η	Bridge Configuration	Type of Modulation	Complexity
[44]	96.60%	2.2kW	Half Bridge	TRM+TZM	Moderate
[51]	>90%	40kW	Full Bridge	TRM+TZM	Simple
[71]	94.60%	300W	Bridgeless	TRM+TZM	Moderate
[114]	97.5%	400W	Full Bridge	TRM+TZM	Moderate
[120]	89.96%	1.35kW	Full Bridge	TRM	Simple
[146]	88.84%	1.38kW	Full Bridge	TRM	Simple
Proposed	96.19%	500W	Full Bridge	TRM	Simple

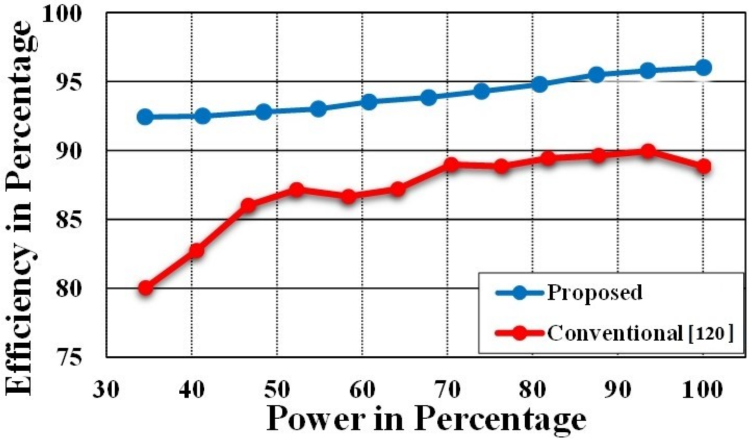

Figure 2.15: Efficiency comparison between conventional [120] (🟥) and the proposed modulation technique (🟦).

techniques result in mild fluctuation in the efficiency vs power curve over the whole operating range and result in loss of soft switching of ac side switches at a relatively low current due to the presence of nonideal effects like voltage drop across the switches and the presence of finite magnetizing current. In [51], a modulation technique for matrix-type DAB is proposed, which offers 70-80% efficiency at lower input voltage and goes up to 90% at higher input voltages. In [71], variable frequency modulation is proposed for a bridgeless DAB converter that operates in two modes over a half cycle of AC, having two DoF. However, the voltage stress on the switches is high for higher wattage. An efficiency comparison between the proposed and conventional TRM modulation is shown in Fig. 2.15. The maximum efficiency using the proposed method 1 is found to be 96.19%.

2.6 Conclusion

In this chapter, a TRM based variable frequency modulation technique for matrix-type DAB is proposed that can be realized using two methods. In method one, 50% gating signal is provided to the AC side bridge and one leg of the DC side bridge without any phase shift. However, there exists a C2C phase shift between the gating signal of the two legs of the DC side bridge, where one leg of DC side bridge is operating at 50% duty cycle and the other operating at sinusoidally modified variable frequency PWM. In method 2, instead of providing a C2C phase shift between the two legs of the DC side bridge, a phase shift exists between switches operating at 50% duty. DSP-based digital realization of both methods is elaborated in detail using a single carrier, which further reduces realization complexity and has the advantage over other complex multi-carrier based modulation techniques or multi-architecture-based MCUs. Simulation results followed by experimental validation of 500W prototype for V2H and G2V application using method one is presented, which offers true ZCS for the AC side bridges over the wide envelope of the line frequency, ZVS turn ON and ZCS turn OFF for the DC side switches, near unity power factor, bidirectional power flow. The maximum efficiency with the proposed technique is found to be 96.19%.

The next chapter explores Q1S AC-DC DAB, focusing on maintaining performance while further reducing computational complexity. It examines the use of an asymmetrical switching sequence-based TRM, showing how minimizing distinct PWM signals simplifies control strategies. The discussion highlights the importance of proposed modulation techniques with the chosen topology to enhance control efficiency and achieve better performance. Implemented on the Texas Instruments TMS320F28335 microcontroller, this approach improves efficiency while preserving soft-switching performance and power quality observed in method 1, setting a new standard in modulation design.